SUPPLEMENTARY INFORMATION

Chemical valorisation of biomass derived furanics and carboxylic acids over niobium-based catalysts

CONTENT

(I) Chemical structures and abbreviations

Table S1. Chemical structures and abbreviations of the reaction products for the different substrates.

Substrate	**Products**		
	Chemical Structure	**Name**	**Abbreviation**
Furfural (Fur)	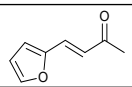	4-(furan-2-yl)but-3-en-2-one	C8
	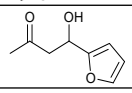	4-(furan-2-yl)-4-hydroxybutan-2-one	C8OH
	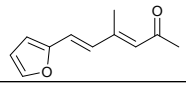	6-(furan-2-yl)-4-methylhexa-3,5-dien-2-one	C11
	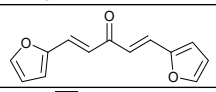	1,5-di(furan-2-yl)penta-1,4-dien-3-one	C13
	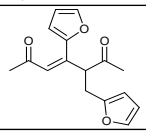	4-(furan-2-yl)-5-(furan-2-ylmethyl)hept-3-ene-2,6-dione	C16
α-Angelica lactone (AnL)	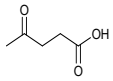	levulinic acid	LA
	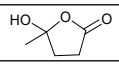	5-hydroxy-5-methyldihydrofuran-2(3H)-one	PseudoLA
	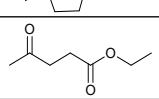	ethyl levulinate	EL
Levulinic acid (LA)	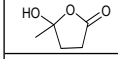	5-hydroxy-5-methyldihydrofuran-2(3H)-one	PseudoLA
	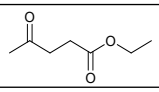	ethyl levulinate	EL
Valeric acid (VA)	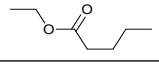	ethyl valerate	EV

Table S2. Chemical structures and abbreviations of the (reactive) solvent decomposition products.

Solvent	Products		
	Chemical Structure	**Name**	**Abbreviation**
Acetone		4-hydroxy-4-methylpentan-2-one	MPOH
		4-methylpent-3-en-2-one	MP
	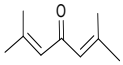	2,6-dimethylhepta-2,5-dien-4-one	DHP
		3,5,5-trimethylcyclohex-2-enone	TCH
		mesitylene	
Ethanol	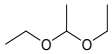	1,1-diethoxyethane	
	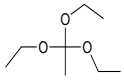	1,1,1-triethoxyethane	

(II) <u>Molecular dimensions of the products of Fur-acetone condensation</u>

Table S3. Calculated molecular dimensions of the products of Fur-acetone condensation reaction system (using the Olex program available at https://www.olexsys.org/olex2/docs/getting-started/installing-olex2/).

Molecule	Spacing box dimension (Å^3)	Spacing box volume (Å^3)	Molecular Surface area (Å^2)	Molecular Volume (Å^3)
C8	4.023×6.328×10.396	264.652	157.98	119.99
C13	3.765×7.343×15.785	429.415	228.31	181.00
C16	8.275×9.333×12.069	931.978	267.59	225.10

<u>(III) Characteristics of the materials</u>

Table S4. Characteristics of the SiNbx nanomaterials.[1]

Sample	**Nb (at.%)[a]**	**S_{BET} (m^2 g^{-1})[b]**	**Pore width (nm)**	**Total acid sites (μmol g^{-1})[c]**	**L/B[d]**
SiNb7	7	913	7	138	1.8
SiNb20	20	682	19	195	2.4
SiNb42	42	449	26	267	2.9
SiNb65	65	296	27	252	3.1
SiNb82	82	224	17	156	3.7

[a] The remaining amount is at.% Si (at.% Nb + at.% Si = 100 %).[1] [b] BET specific surface area.[1] [c] Total Lewis (L) plus Brønsted (B) acid sites.[1] [d] Molar ratio L/B.

(IV) <u>Characterization of TUD-1 and Nb_2O_5/TUD-1</u>

The high angle PXRD patterns of TUD-1 and Nb_2O_5/TUD-1 showed a very broad beak at *ca.* 22.7° 2θ, which is consistent with the TUD-1 mesoporous structure (three-dimensional, sponge-like structure) formed by amorphous pore walls (Figure S1A).[2] Bulk Nb_2O_5 exhibited a broad peak at *ca.* 23.1° 2θ, associated with the very small nanoparticles of this material, and in agreement with the literature.[1] On the other hand, the low angle PXRD patterns of TUD-1 and Nb_2O_5/TUD-1 showed a broad peak centred at *ca.* 0.8 and 0.9° 2θ, respectively, associated with a mesoporous system (Figure S1B), characteristic of TUD-1 type materials.[3,4] Bulk Nb_2O_5 nanoparticles exhibited a weak broad peak centred at *ca.* 1.1 ° 2θ, which may be related to interparticle mesoporosity (Figure S1A,B).

The isotherms of TUD-1 and Nb_2O_5/TUD-1 presented type IV features with a hysteresis loop at p/p_0 greater than 0.7 and 0.5, respectively (Figure S2C), which is characteristic of mesoporous materials of the type TUD-1.[5–7] The specific surface area (S_{BET}) and pore sizes (d_p, Figure S2D) of the composite

Nb_2O_5/TUD-1 were 490 $m^2\ g^{-1}$ and 4-10 nm, respectively, and the TUD-1 silica possessed 471 $m^2\ g^{-1}$ and 11-18 nm.[8] These results may be due to the introduction of Nb_2O_5 in the mesoporous siliceous matrix. Bulk Nb_2O_5 (1.5 – 5 nm nanoparticle sizes) possessed lower S_{BET} of 161 $m^2\ g^{-1}$.[1]

The SEM image of Nb_2O_5/TUD-1 (Figure S2(b) and (c)) showed particles of irregular size (micrometres) and shape. The TEM images of Nb_2O_5/TUD-1 (Figure S2(f) and (g)) showed a sponge- or worm-like mesoporous matrix with some dark grey domains which may be attributed to the embedded Nb_2O_5 nanoparticles.

The elemental mappings (SEM, EDS) suggested somewhat uniform Si and Nb distributions. On the other hand, the STEM images (Figure S2(h) and (i)) showed regions with uniform Si and Nb distributions, and some small domains rich in Nb (*ca.* 20 nm size) which may be small aggregates of Nb_2O_5 nanoparticles.

Overall, the above results suggested that Nb_2O_5/TUD-1 is a composite of an amorphous mesoporous matrix and isolated or aggregated Nb_2O_5 nanoparticles in the surrounding mesoporous matrix.

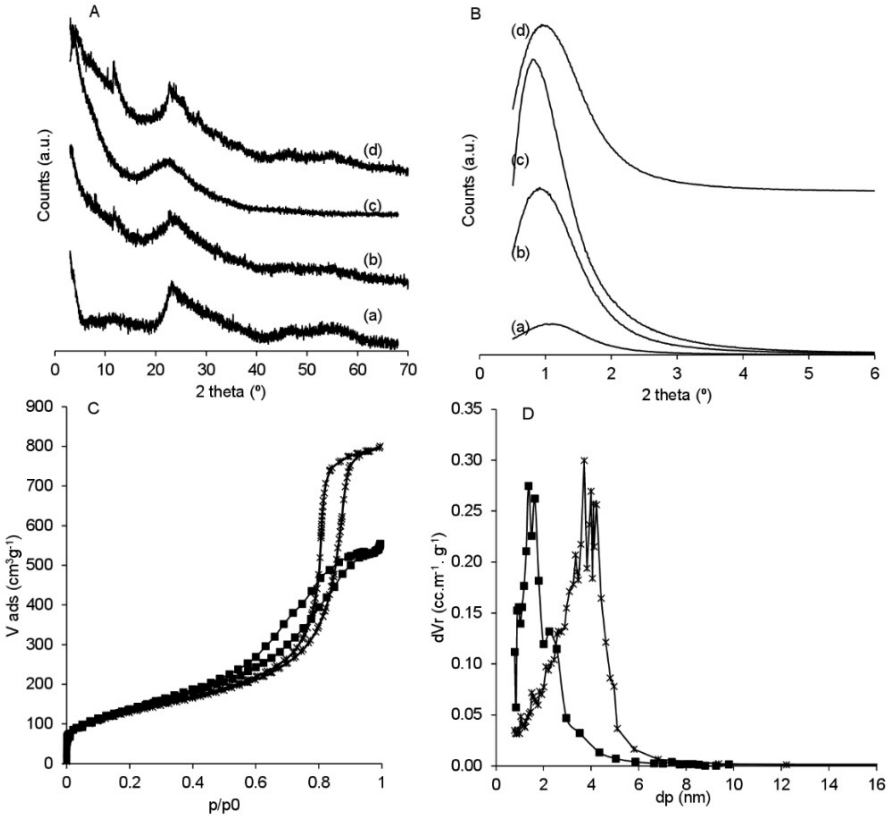

Figure S1. Wide angle (A) and low angle (B) powder X-ray diffraction patterns of Nb_2O_5 (a), Nb_2O_5/TUD-1 (b) and TUD-1 (c). The data for the used Nb_2O_5/TUD-1 ((d) in (A) and (B)) are included. N_2 sorption isotherms at -196 °C (C) and pore size distribution curves (D) of Nb_2O_5/TUD-1 (■) and TUD-1 (*).

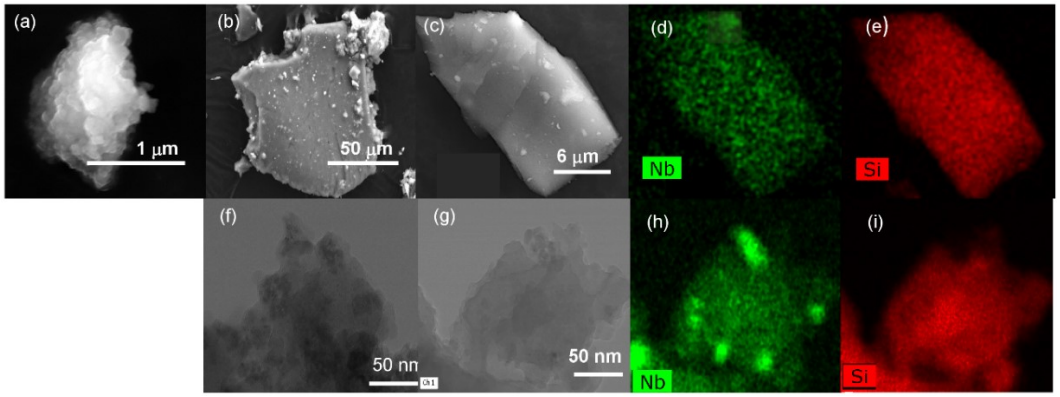

Figure S2. SEM of Nb_2O_5 (a) and Nb_2O_5/TUD-1 ((b) and (c)) and the corresponding elemental mappings (Nb (green (d)); Si (red (e))).TEM images of Nb_2O_5/TUD-1 ((f) and (g)) and the corresponding STEM images (Nb (green (h)); Si (red (i))).

Stability of Nb_2O_5/TUD-1 and Nb_2O_5

For comparative studies to SiNb65, bulk Nb_2O_5 was calcined at 400 °C prior to reuse. Nb_2O_5 suffered partial loss of activity, *i.e.*, Fur conversion decreased from run 1 (45 %) to run 2 (36 %) and C8 dropped from 28 % to 23 % at 140 ºC/5 h (Figure S3A). The used Nb_2O_5 solid exhibited a similar PXRD pattern (Figure S10) and morphology (TEM, Figure S3B)) to the fresh catalyst. However, S_{BET} of the used catalyst was 0.92 of that for the original catalyst. Possibly, the nanoparticles became more aggregated.
Although calcination at 400 ºC was sufficient for recycling SiNb65, this was not the case of the composite Nb_2O_5/TUD-1. While the original composite material was pristine white, the respective used solid was brown in colour due to adsorbed carbonaceous matter, requiring calcination at 600 ºC to restore the characteristic white colour (calcination at 400 ºC was insufficient, leading to a light brown coloured solid). This seems to constitute another advantage of the SiNbx type catalysts which require milder thermal regeneration conditions (lower energy consumption) compared to the Nb_2O_5/TUD-1 composite. The used Nb_2O_5/TUD-1 solid possessed a higher amount of carbonaceous matter (19 wt.% C based on elemental analysis) than used SiNb20 (8 wt.% C). On the other hand, Nb_2O_5/TUD-1 suffered partial loss of activity; Fur conversion decreased from run 1 (45 %) to run 2 (40 %) and C8 dropped from 32 % to 27 % (and total yield dropped from 42 % to 36 %) at 140 ºC/5 h (Figure S3A). The original and used composite solids exhibited a similar PXRD patterns (Figure S1A and S1B) and morphology (irregular size and shape, based on SEM, Figure S3C), and no drop of S_{BET} was observed (the used solid possessed S_{BET} = 522 m^2 g^{-1}).
Contact tests (140 ºC) were carried out for Nb_2O_5/TUD-1 and Nb_2O_5 in similar fashions to that described for SiNb65 (after catalyst filtration at 5 h, Fur was added (1.6 M) and left to react for another 5 h). The Fur conversion did not surpass 5 % in both cases, suggesting that the loss of activity is not related to leached active Nb species. The factors responsible for the deactivation of Nb_2O_5/TUD-1 are not clear at this stage.

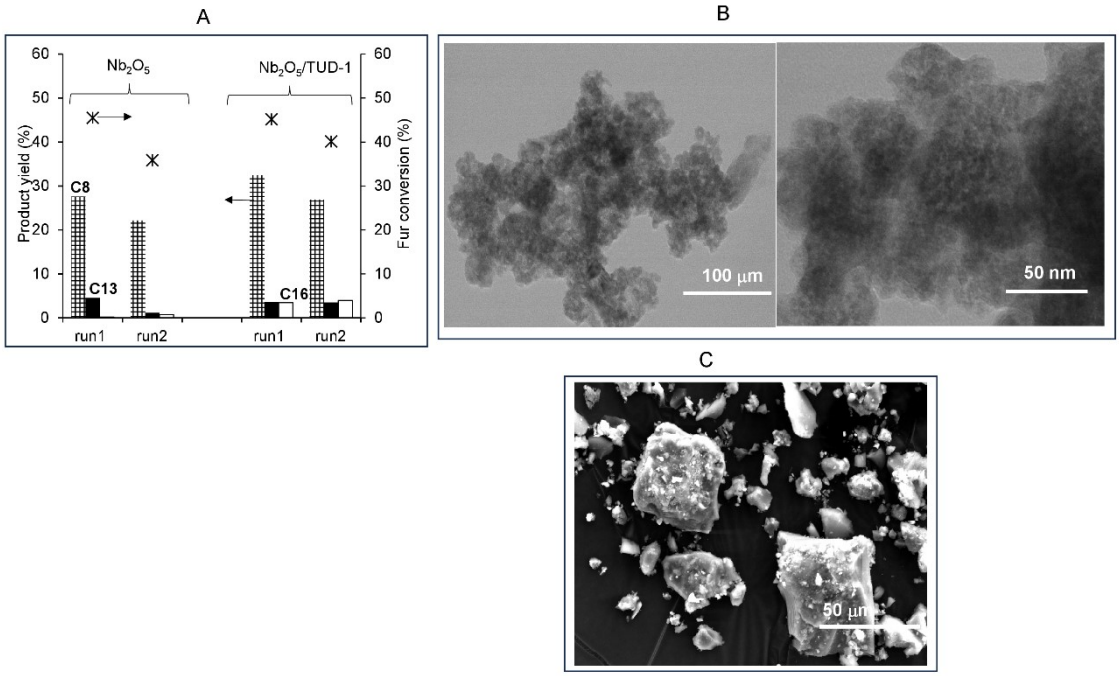

Figure S3. (A) Recycling runs for Fur/acetone condensation in the presence of Nb_2O_5 and Nb_2O_5/TUD-1 Fur conversion (*) and yield of C8 (stripped bars), C13 (black bars) and C16 (black bars); C8OH and C11 yields were always less than 2 %. Reaction conditions: 1.6 M Fur in acetone, 140 °C, 29.7 g_{cat} L^{-1}, 5 h. (B) STEM image of used Nb_2O_5 (left side) and SiNb65 (right side). (C) SEM image of used Nb_2O_5/TUD-1.

(V) Characterization of commercial Nb_2O_5-com

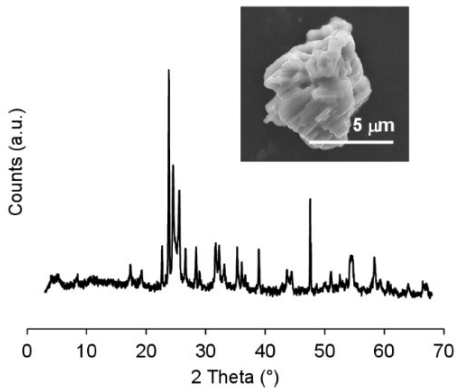

Figure S4. PXRD pattern and SEM image (inset) of commercial Nb_2O_5-com. This material consisted essentially of the monoclinic crystal phase (PDF card number 04-007-0450).

(VI) Material (carbon) balances

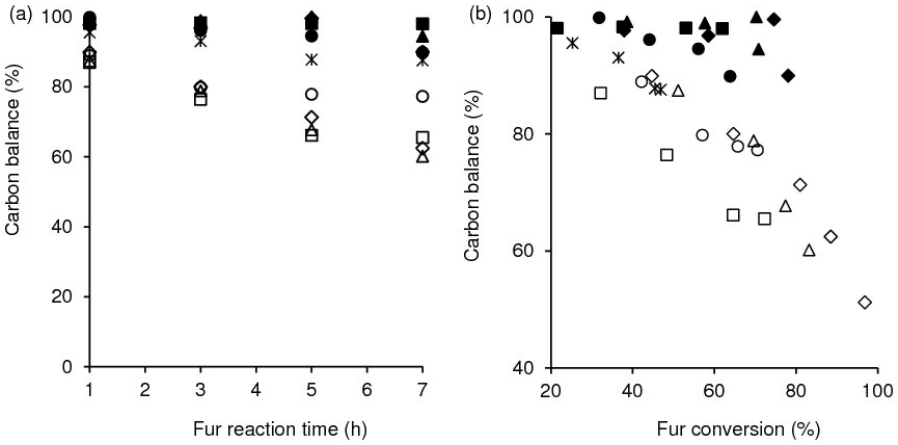

Figure S5. Dependency on Fur reaction time (a) or Fur conversion (b) of the carbon balance (considering Fur and C8-C16 products) for the non-calcined materials SiNbx (open symbols) and calcined materials SiNbx (solid symbols) with x = 20 (squares), 42 (diamonds), 65 (triangles) and 82 (circles) and Nb_2O_5 (*). Reaction conditions: 1.6 M Fur in acetone, 140 °C, 29.7 g_{cat} L^{-1}.

(VII) Kinetic modelling

Kinetic model B considering first and second order reactions for the Fur/acetone system:
The kinetic model B is like the kinetic model A described in the main text, albeit instead of equations (4), (6) and (7), model B contemplates equations (4a), (6a) and (7a), respectively. The values of the rate constants (Table S4) were similar to those obtained by the kinetic model A (Table 1). Since acetone was used in excess (solvent), its concentration may be considered approximately constant.

$$\frac{V}{W}\frac{dC_{C8}}{dt} = k_2\, C_{C8OH} - \left(k_3 + k_4 C_{Fur} + k_5 C_{C8} + k_9\right) C_{C8} \qquad \text{Eq. (4a)}$$

$$\frac{V}{W}\frac{dC_{C13}}{dt} = k_4\, C_{C8} C_{Fur} - k_7\, C_{C13} \qquad \text{Eq. (6a)}$$

$$\frac{V}{W}\frac{dC_{C16}}{dt} = 0.5\, k_5 C_8^2 - k_8\, C_{C16} \qquad \text{Eq. (7a)}$$

Table S5. Model B: Kinetic constants (considering first and some second order reactions) and objective function values for Fur/acetone condensation, in the presence of the niobium-based nanocatalysts, at 140 °C.

Rate Constant[a]	Step	SiNb20	SiNb42	SiNb65	SiNb82	Nb_2O_5
k_1	FUR-C8OH	5.120×10^{-3}	1.083×10^{-2}	1.020×10^{-2}	6.474×10^{-3}	4.582×10^{-3}
k_2	C8OH-C8	1.442×10^{3}	1.452×10^{3}	1.442×10^{3}	1.442×10^{3}	1.442×10^{3}
k_3	C8-C11	1.555×10^{-7}	2.206×10^{-4}	1.156×10^{-6}	6.857×10^{-8}	1.513×10^{-10}
k_4	C8-C13	2.002×10^{-3}	3.432×10^{-3}	1.836×10^{-3}	2.296×10^{-3}	1.015×10^{-3}
k_5	C8-C16	3.326×10^{-3}	1.776×10^{-3}	3.471×10^{-3}	4.452×10^{-3}	1.681×10^{-2}
k_6	FUR-BP1	1.738×10^{-8}	1.002×10^{-7}	7.406×10^{-8}	2.509×10^{-9}	5.743×10^{-12}
k_7	C13-BP2	4.067×10^{-3}	5.693×10^{-3}	2.463×10^{-5}	5.945×10^{-3}	6.898×10^{-3}
k_8	C16-BP3	2.856×10^{-4}	1.569×10^{-2}	1.037×10^{-1}	6.883×10^{-2}	4.210×10^{-1}
k_9	C8-BP4	1.555×10^{-7}	2.206×10^{-4}	1.156×10^{-6}	6.857×10^{-8}	1.513×10^{-10}
k_{10}	C11-BP5	6.786×10^{3}	6.788×10^{3}	6.786×10^{3}	6.786×10^{3}	6.786×10^{3}
F_{obj}		0.0288	0.184	0.249	0.2087	0.1064

[a] The values of k_i are expressed as (L g_{cat}^{-1} h^{-1}), except for k_4 and k_5 which are expressed as (L g_{cat}^{-1} h^{-1} M^{-1}).

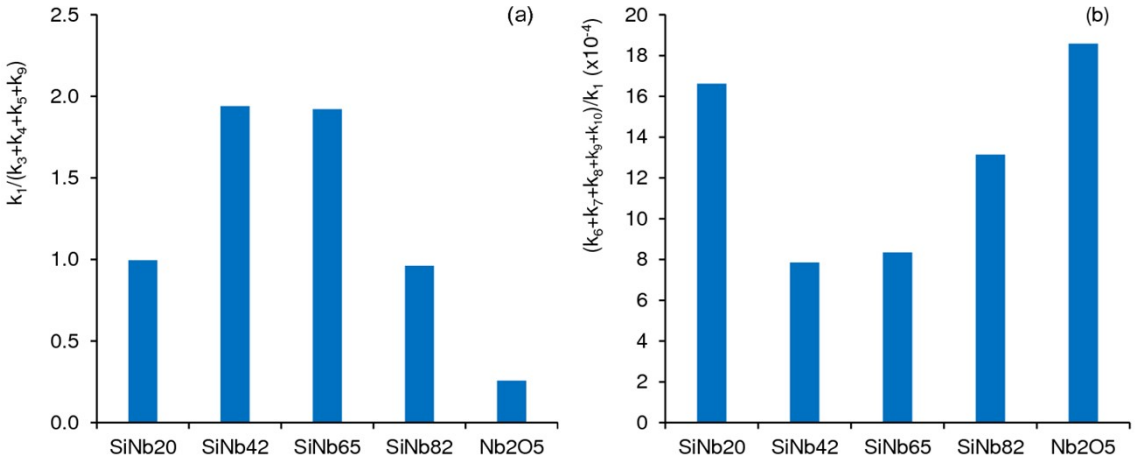

Figure S6. Model B: Ratio of rate constants (a) reflecting a favourable C8 formation (higher ratio $k_1/(k_3+k_4+k_5+k_9)$), or (b) enhanced decomposition paths of C8 and remaining bioproducts to unknown byproducts (higher ratio $(k_6+k_7+k_8+k_9+k_{10})/k_1$). Reaction conditions: 1.6 M Fur in acetone, 140 °C, 29.7 g_{cat} L^{-1}.

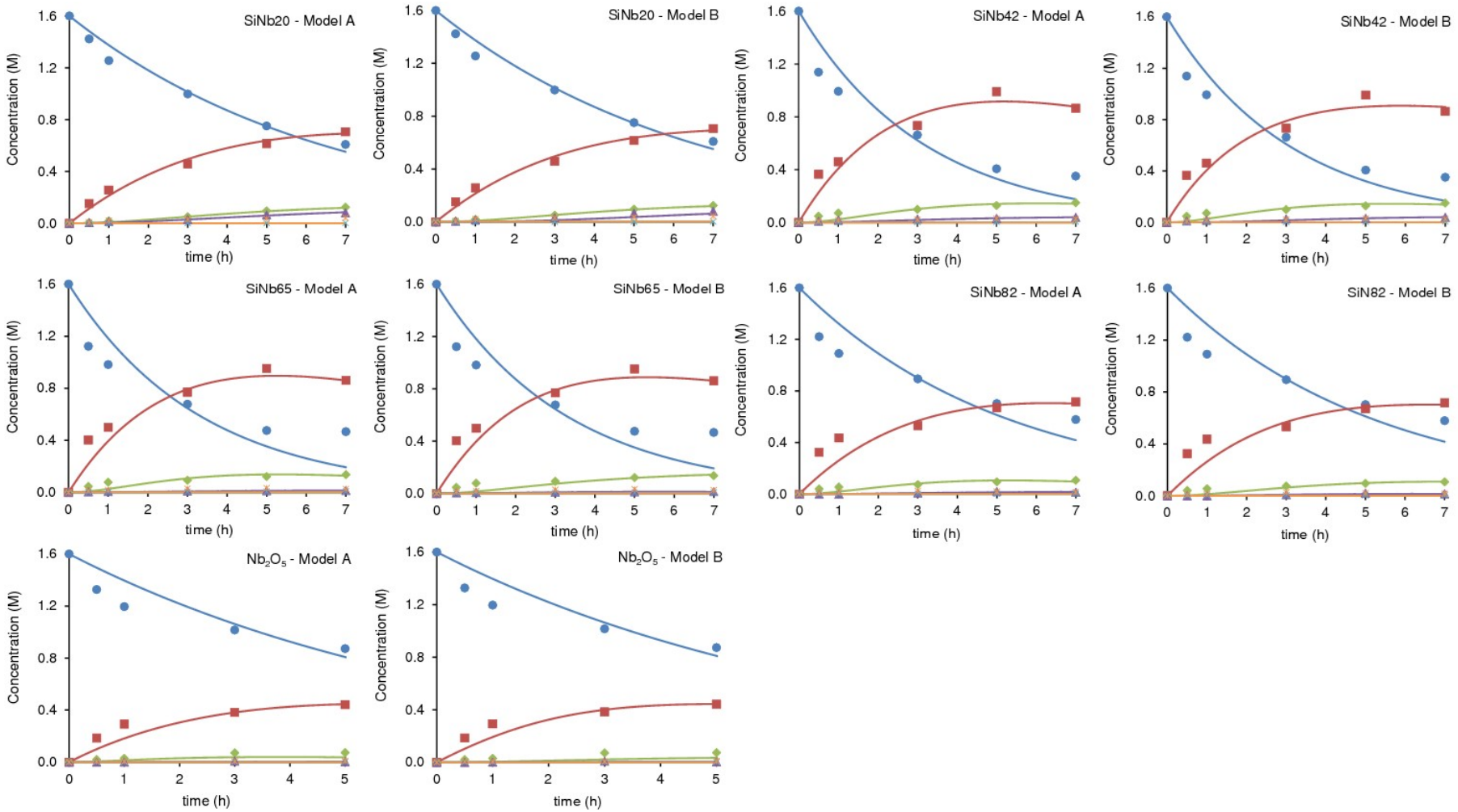

Figure S7. Calculated kinetic curves for Fur/acetone condensation in the presence of the nanomaterials SiNbx and Nb_2O_5, using the kinetic model A or model B. Reaction conditions: 1.6 M Fur in acetone, 140 °C, 29.7 g_{cat} L^{-1}. The models were fitted to the experimental results until 7 h (exceptionally until 5 h for Nb_2O_5 due to apparent deactivation after this reaction time).

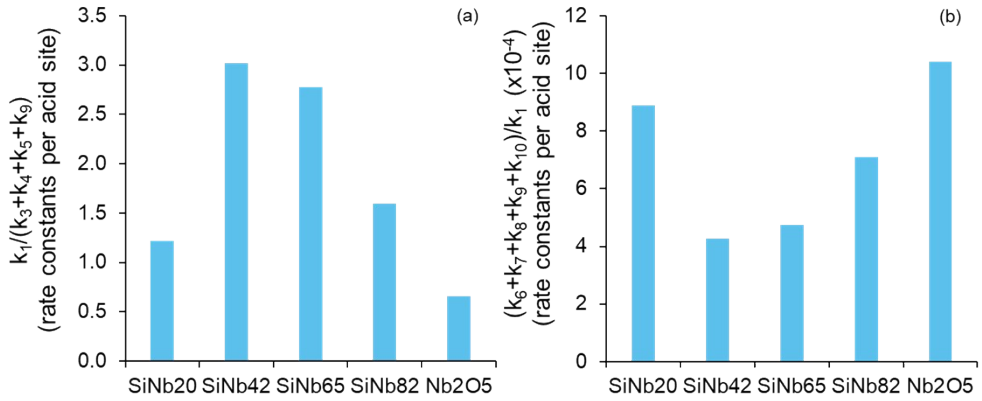

Figure S8. Ratio of rate constants (a) reflecting a favourable C8 formation (higher ratio $k_1/(k_3+k_4+k_5+k_9)$), or (b) enhanced decomposition paths to byproducts (higher ratio $(k_6+k_7+k_8+k_9+k_{10})/k_1$). The *ki* values are expressed per acid sites (AS), *i.e.*, (L mol_{AS}^{-1} h^{-1}), taking into consideration the total amount of AS of each catalyst (Table S4). Reaction conditions: 1.6 M Fur in acetone, 140 °C, 29.7 g_{cat} L^{-1}.

(VIII) Products of acetone decomposition

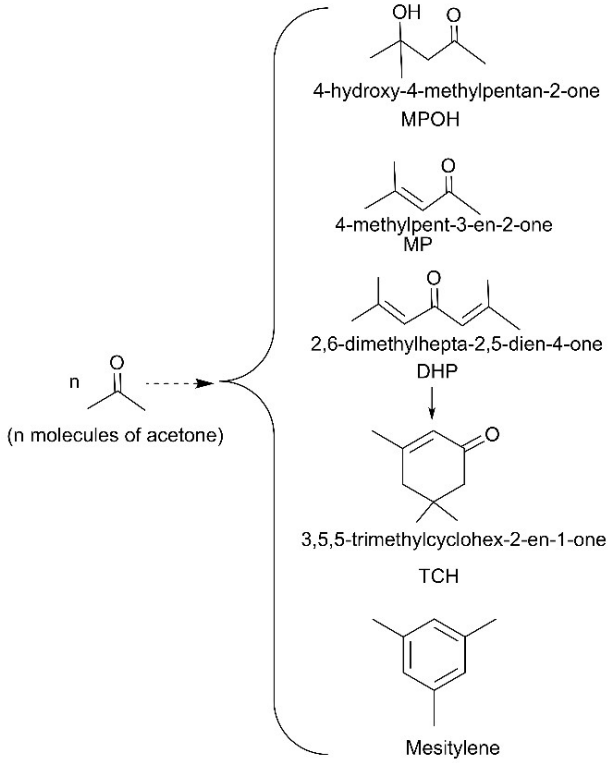

Scheme S1. Acetone decomposition products formed in the Fur/acetone condensation, in the presence of SiNbx, at 140 °C (initial mole ratio acetone:Fur ≅ 8).

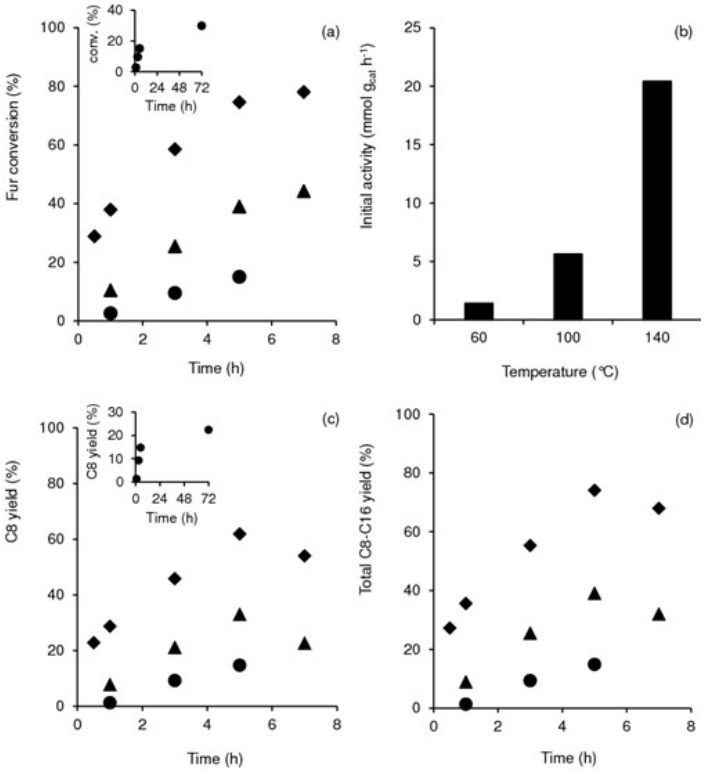

Figure S9. Influence of the of Fur-acetone condensation reaction temperature on conversion (a), initial activity (b), C8 yield (c) and total C8-C16 products yield (d), in the presence of SiNb42; 60 °C (●), 100 °C (▲) and 140 °C (♦). The insets of (a, c) show the catalytic results up to 72 h for the reaction at 60 °C. Reaction conditions: 1.6 M Fur in acetone, 29.7 g_{cat} L^{-1}.

(IX) <u>Characterization of used solids</u>

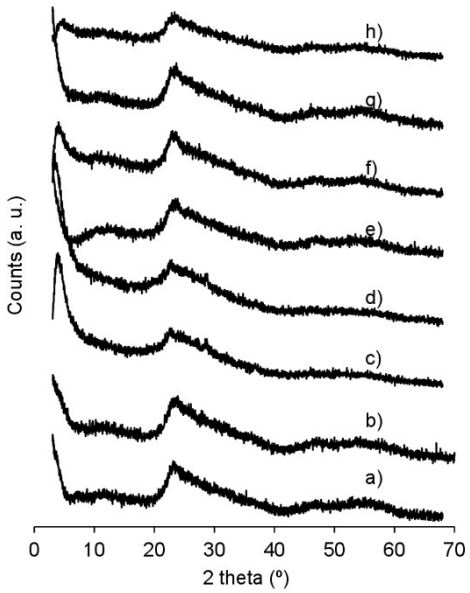

Figure S10. PXRD patterns of SiNb65 before (e) and after use (f). The results are also given for Nb_2O_5 (a, b), SiNb20 (c, d) and SiNb82 (g, h), showing no significant structural differences between the respective fresh (a, c, e, g) and used (b, d, f and h) solids. The results for SiNb42 are given in ref.[1] Reaction conditions: 1.6 M Fur in acetone, 140 °C, 29.7 g_{cat} L^{-1}.

(X) <u>Catalyst stability (AnL). Water effect (AnL, LA, VA).</u>

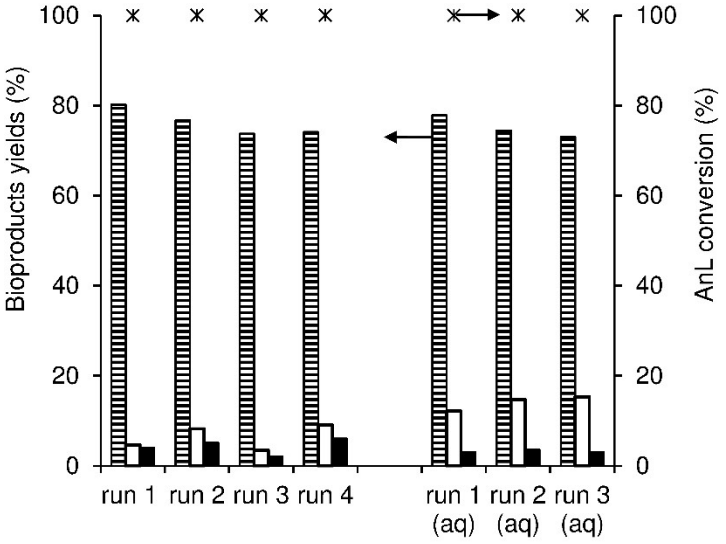

Figure S11. Consecutive batch runs of AnL reaction (without adding water (runs 1-4)) and, on the other hand, with the addition of 5 mol% water to the reaction mixture (runs 1-3 (aq)), in the presence of SiNb42; AnL conversion (*) and yields of EL (stripped bars), LA (white bars) and pseudoLA (black bars). Reaction conditions: 0.35 M AnL in ethanol, 10 g_{cat} L^{-1}, 3 h, 140 °C.

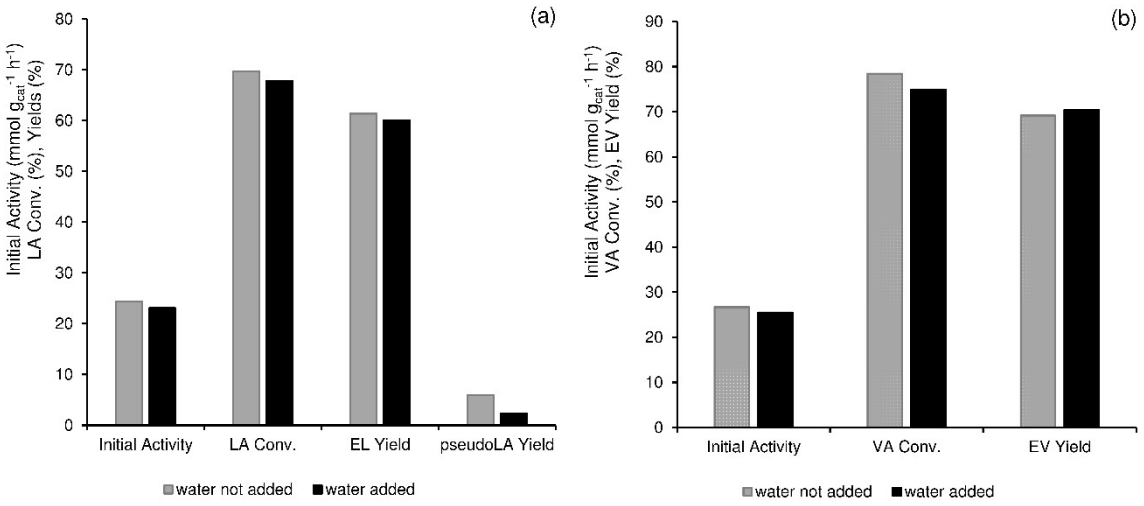

Figure S12. Influence of adding 5 mol% water (black bars) to the LA (a) and VA (b) reactions; the results for the reactions without adding water (grey bars) are given for comparisons. Reaction conditions: 0.35 M substrate in ethanol, 10 g_{cat} L^{-1}, 1 h, 140 °C.

(XI) Comparison of catalytic results for SiNb50 in Fur/acetone condensation to literature data

TableS6. Catalytic results for SiNb42 and literature data for SiOx-based fully inorganic solid catalysts, tested for the Fur-acetone condensation reaction[1,9–21]

	Catalyst	Acet:Fur [a]	Solvent [a]	T (°C) [a]	T (h) [a]	Cat:Fur (m/m)	$[Fur]_0$ (M) [a]	Conversion (%)	Products yield (%)			Ref
									C8	C13	others	
1	SiNb42	7.6	-	60	5/72	0.20	1.56	30	15/22	-/1	1 (C16)	-
2	SiNb42	7.6	-	100	5	0.20	1.56	40	32	3	2 (C8OH), 2 (C16)	-
3	SiNb42	7.6	-	140	5	0.20	1.56	75	62	8	2 (C8OH), 2(C16)	[1]
4	SiNb42	7.6	-	160	5	0.20	1.56	100	71	18	1 (C11), 1 (C16)	-
5	2.6Nb-MFI	10	-	140/160	2	0.83	1.21	50/87	50/80	-/-	nm	[9]
6	Sn-MFI	10	-	160	6	0.83	1.24	80	60	-	nm	[14]
7	0.05K-Sn-MFI	10	-	160	0.75	0.83	1.24	93	72	18	nm	[14]
8	Sn-MFI	10	-	160	6	0.83	1.24	80	60	-	nm	[15]
9	H-BEA	10	-	60/100	2	0.31	1.21	35/50	28/38	<1/2	5/8 (C16)	[16]
10	Sn-BEA	10	-	160	2	0.83	1.24	97	40	15	nm	[15]
11	MCM-22	10	-	100	2	0.15	1.21	60	48	4	7 (C16),1 (C8OH)	[17]
12	Ca-ZSM-5	0.8	H_2O	80	2	0.63	4.9	100	40	60	-	[18]
13	1.1K-N-BEA [b]	10	-	100	2	0.31	1.21	80	52	13	12 (C8OH)	[19]
14	K-IMP-FAU(15) [c]	10	-	100	nm	0.31	1.21	45	14	7	20 (C8OH)	[20]
15	MK-Y [d]	10	-	160	1	0.31	1.21	95 [i]	95 [i]	-	nm [i]	[21]
16	MK-L [e]	10	-	160	1	0.31	1.21	95 [i]	95 [i]	-	nm [i]	[21]
17	$20K_2O/12wt\%MgAl$-SBA-15 [f]	5.0	-	50	3/24	0.08	2.21	83/99	19/42	19/28	47/30 (C8OH)	[10]
18	Zr_{25}/m-SiO_2 [g]	10	-	140	2	0.42	1.21	100	76	13	4 (C8OH)	[11]
19	SiO_2@MgAl core shell LDH [h]	10	-	50	4	0.16	1.21	28	7	1	18 (C8OH)	[12]
20	Cu/Al-MCM-41	40	-	175	24			98	92			[13]

[a] Acet:Fur = mole ratio of acetone:Fur, Solvent other than Fur and acetone, T = reaction temperature, t = reaction time (nm = not mentioned), $[Fur]_0$ = initial Fur concentration, Others = other products formed in yields of at least 1 %. [b] 1.1K-N-BEA= Zeolite BEA after impregnation with KNO_3, filtration and not washed. [c] K-IMP-FAU(15)= Zeolite Faujasite impregnated with KNO_3 (for this catalyst catalytic stability was not reported). [d] MK-Y= Hierarchical Y washed with KNO_3. [e] MK-L= Hierarchical L washed with KNO_3,[f] For this catalyst the activity decreased in consecutive runs. [g] Zr_{25}/m-SiO_2 = zirconium (25 wt%) on mesoporous silica. [h] LDH= layered double hydroxide. [I] The precise values are not given.

(XII) Comparison of catalytic results for SiNb42 with different substrates to literature data

Table S7. Catalytic results for SiNb50 and literature data for fully inorganic SiOx based solid catalysts, tested for the AnL/ethanol conversion.[22,23]

	Catalyst	T (°C) [a]	t (h) [a]	Cat:AnL (m/m)	$[AnL]_0$ (M) [a]	Conv. (%) [a]	Products yield (%)		Ref
							LA+pseudoLA	EL [a]	
1	SiNb42	140	1/7	0.28	0.35	100/100	15/22	70/90	-
2	SiNb42	110	1	0.28	0.35	96	32	58	-
3	($HClO_4$-SiO_2)	90	2	0.04	0.25	100	62	91	22
4	H-Beta-14.5 [b]	110	1.5	0.4	0.28	95	71	10	23

[a] T = reaction temperature, t = reaction time, $[AnL]_0$ = initial AnL concentration, Conv. = AnL conversion, EL = ethyl levulinate. [b] Beta zeolite with Si/Al molar ratio of 14.5.

Table S8. Catalytic results for SiNb42 and literature data for fully inorganic (non-carbon) silica based catalysts, tested for the LA/ethanol esterification.[24–38]

	Catalyst	T (°C) [a]	t (h) [a]	Cat:LA (m/m)	$[LA]_0$ (M) [a]	Conv. (%) [b]	EL yield (%)	Ref
1	SiNb42	140	1/7	0.24	0.35	70/100	61/100	-
2	HT-SBA-15 [c]	110	5	0.03	1.19	75	74	24
3	V	75	5	0.2	1.46	88	88	25
4	S-Zr-SBA-15(10.7) [e]	70	24	0.05	1.46	80	nm [f]	31
5	Zr-SBA-15	78	5	0.29	0.57	85	85	32
6	3wt.%WO_3-SBA-16 (continuous flow)	250	(2 $mL_{LA+ethanol}\,h^{-1}\,g_{cat}^{-1}$)	4.31	1.96	100	95	33
7	HPW-MCM-41	80	10	0.25	2.54	75	nm [f]	34
8	HSiW/MCM-41	80	10	0.25	1.46	85	nm [f]	35
9	SiO_2-SO_3H	70	4	0.06	1.70	68	68	36
10	Sulfated SiO_2	78	4	0.3	0.79	nm [f]	53	37
11	$HClO_4$-SiO_2	100	5	0.10	0.20	nm	99	38
12	$H_4SiW_{12}O_{40}/SiO_2$	75	6	0.4	0.25	93	60	26
13	Zr-KIL-2 [g]	70	7	0.025	2.54	55	nm [f]	27
14	2.5SiO_2-ZrO_2	70	10	0.10	1.46	77	nm [f]	28
15	30% CeTPA/SGP [h] (continuous flow)	140	(1 $mL_{LA+ethanol}\,h^{-1}\,mL_{cat}^{-1}$)	-	1.76	55	55	29
16	STA-SGC [i]	85	4	0.20	1.76	nm [f]	98	30

[a] T = reaction temperature, t = reaction time, $[AnL]_0$ = initial AnL concentration. [b] Conv. = LA conversion. [c] HT-SBA-15 = hydrotalcite SBA-15. [d] STA = Silicotungstic acid. [e] S-Zr-SBA-15(10.7) = Sulfated mesoporous zirconosilicate. [f] nm = not mentioned. [g] KIL-2 = type of mesostructured silica. [h] 30%CeTPA/SGP = cerium salt of phosphotungstic acid supported on commercially silica gel pellets. [i] STA-SGC = silicotungstic acid on silica gel spheres.

Table S9 Catalytic results for SiNb42 and literature data for fully inorganic SiOx-based solid catalysts, tested for the VA/ethanol esterification.[39,40]

	Catalyst	T (°C) [a]	t (h) [a]	Cat:VA (m/m)	$[VA]_0$ (M) [a]	Conv. (%) [a]	EV yield (%) [a]	Ref
1	SiNb42	140	1/3	0.28	0.35	78/100	69/91	-
2	SiNb42	140	1/3/16	0.54	0.43	73/82/99	71/80/98	-
3	SiNb42	140	24	0.28	0.83	99	72	-
4	0.5Nb-Al-SBA-15	150(MW irradiation)	0.25	0.54	0.43	35	nm [b)]	39
5	F10%/Al-SBA-15 [c]	150(MW irradiation)	0.25	0.54	0.43	55	nm [b)]	39
6	30% PTA/Al-SB [d]	100	3	- [f]	2.17	96	96	40
7	30%PTA/Al-SBA-15 [e]	100	3	- [f]	2.17	92	92	40
8	30%PTA/MCM-41 [e]	100	3	- [f]	2.17	88	88	40
9	30%PTA/MCM-48 [e]	100	3	- [f]	2.17	91	91	40
10	30%PTA/KIT-5 [e]	100	3	- [f]	2.17	85	85	40
11	30%PTA/KIT-6 [e]	100	3	- [f]	2.17	80	80	40

[a] T = reaction temperature, t = reaction time, $[VA]_0$ = initial VA concentration, Conv. = VA conversion. [b] nm = not mentioned; [c] F10% = 10 % fluoride (using NH_4F) in the material synthesis. [d] PTA/Al-SB = Phosphotungstic acid supported on Al-SBA-15. [f] Insufficient details for calculating the mass of VA or reaction mixture per mass of catalyst, compromising comparisons (given: 100 mg catalyst, molar ratio VA:ethanol = 1:6).

References

1 K. Skrodczky, M. M. Antunes, Q. Zhu, A. A. Valente, N. Pinna and P. A. Russo, *Nanomaterials*, 2023, **13**, 3046.
2 S. Telalović, A. Ramanathan, G. Mul and U. Hanefeld, *J. Mater. Chem.*, 2010, **20**, 642–658.
3 R. Anand, R. Maheswari and U. Hanefeld, *J. Catal.*, 2006, **242**, 82–91.
4 S. Telalović, A. Ramanathan, J. F. Ng, R. Maheswari, C. Kwakernaak, F. Soulimani, H. C. Brouwer, G. K. Chuah, B. M. Weckhuysen and U. Hanefeld, *Chem. - A Eur. J.*, 2011, **17**, 2077–2088.
5 C. Simons, U. Hanefeld, I. W. C. E. Arends, R. A. Sheldon and T. Maschmeyer, *Chem. - A Eur. J.*, 2004, **10**, 5829–5835.
6 S. Lima, M. M. Antunes, A. Fernandes, M. Pillinger, M. F. Ribeiro and A. A. Valente, *Appl. Catal. A Gen.*, 2010, **388**, 141–148.
7 M. M. Antunes, P. Neves, A. Fernandes, S. Lima, A. F. Silva, M. F. Ribeiro, C. M. Silva, M. Pillinger and A. A. Valente, *Catal. Sci. Technol.*, 2016, **6**, 7812–7829.
8 D. M. Gomes, P. Neves, M. M. Antunes, A. J. S. Fernandes, M. Pillinger and A. A. Valente, *Catalysts*, 2022, 12.
9 E. Yuan, W. Dai, G. Wu, N. Guan and L. Li, *Microporous Mesoporous Mater.*, 2020, **305**, 110361.
10 M. Arumugam, O. Kikhtyanin, A. Osatiashtiani, V. Kyselová, V. Fila, I. Paterova, K. L. Wong and D. Kubička, *Sustain. Energy Fuels*, 2023, **7**, 3047–3059.
11 R. Balaga, P. Yan, K. Ramineni, H. Du, Z. Xia, M. R. Marri and Z. C. Zhang, *Appl. Catal. A Gen.*, 2022, **648**, 118901.
12 T. Kondratowicz, S. Slang, L. Dubnová, O. Kikhtyanin, P. . Belina and L. Capek, *Appl. Clay Sci.*, 2022, **216**, 106365.
13 P. Gandhi, B. Saha, S. Vedachalam and A. K. Dalai, *Sustain. Energy Fuels*, 2023, 4260–4272.
14 W. Li, M. Su, T. Zhang, Q. Ma and W. Fan, *Fuel*, 2019, **237**, 1281–1290.
15 M. Su, W. Li, T. Zhang, H. S. Xin, S. Li, W. Fan and L. Ma, *Catal. Sci. Technol.*, 2017, **7**, 3555–3561.
16 O. Kikhtyanin, V. Kelbichová, D. Vitvarová, M. Kubů and D. Kubička, *Catal. Today*, 2014, **227**, 154–162.
17 O. Kikhtyanin, P. Chlubná, T. Jindrová and D. Kubicka, *Dalt. Trans.*, 2014, **43**, 10628–10641.
18 X. Fang, Z. Wang, W. Song and S. Li;, *J. Taiwan Inst. Chem. Eng.*, 2020, **108**, 16–22.
19 O. Kikhtyanin, R. Bulánek, K. Frolich, J. Cejka and D. Kubička, *J. Mol. Catal. A Chem.*, 2016, **424**, 358–368.
20 O. Kikhtyanin, Y. Ganjkhanlou, D. Kubička, R. Bulánek and J. Čejka, *Appl. Catal. A Gen.*, 2018, **549**, 8–18.
21 A. Al-Ani, C. Freitas and V. Zholobenko, *Microporous Mesoporous Mater.*, 2016, **293**, 109805.
22 S. B. Onkarappa, N. S. Bhat and S. Dutta, *Biomass Convers. Biorefinery*, 2020, **10**, 849–856.
23 M. Paniagua, J. A. Melero, J. Iglesias, G. Morales, B. Hernándes and C. López-Aguado;, *Appl. Catal. A, Gen.*, 2017, **537**, 74–82.
24 M. Manikandan and P. Sangeetha, *Silicon*, 2022, **14**, 3119–3124.
25 N. Lucas, L. Gurrala and A. Athawale, *J. Porous Mater.*, 2019, **26**, 1335–1343.
26 K. Yan, G. Wu, J. Wen and A. Chen, *Catal. Commun.*, 2013, **34**, 58–63.
27 M. Popova, Á. Szegedi, H. Lazanova, R. Alenka, Y. Kalvachev, G. Atanasova, N. Wilde, N. N. Tusar and R. Gläser, *Microporous Mesoporous Mater.*, 2016, **235**, 50–58.
28 K. Yasutaka, K. Wako, K. Nemoto and T. Fujitani, *Appl. Catal. A, Gen.*, 2014, **476**, 186–196.
29 X. Kong, S. Wu, L. Liu, S. Li and J. Liu, *Mol. Catal.*, 2017, **439**, 180–185.
30 X. Kong, S. Wu, X. Li and J. Liu, *Energy and Fuels*, 2016, **30**, 6500–6504.
31 Y. Kuwahara, T. Fujitani and H. Yamashita, *Catal. Today*, 2014, **237**, 18–28.
32 C. R. Patil and C. V. Rode, *ChemistrySelect*, 2018, **3**, 12504–12511.
33 F. Ciardelli, M. Michelotti, A. Altomare and E. Roland, *J. Mol. Catal. A Chem.*, 2017, **426**, 30–38.
34 M. Wu, Z. Qing-Qing, J. Li, X.-L. Su, H.-Y. Wu, X.-X. Guan and X.-C. Zheng, *J. Porous Mater.*, 2016, **23**, 1329–1338.

35 Y. Chen, X. Zhang, M. Dong, Y. Wu, G. Zheng, J. Huang, X. Guan and X. Zheng, *J. Taiwan Inst. Chem. Eng.*, 2016, **61**, 147–155.
36 D. D. Ristiana, S. Suyanta and N. Nuryono, *Mater. Today Commun.*, 2022, **32**, 103953.
37 N. A. S. Ramli, N. I. Hisham and N. A. S. Amin, *Sains Malaysiana*, 2018, **47**, 1131–1138.
38 F. Yang and J. Tang, *ChemistrySelect*, 2019, **4**, 1403–1409.
39 M. Blanco-Sánchez, E. Pfab, N. Lázaro, A. M. Balu, R. Luque and A. Pineda, *Front. Chem.*, , DOI:10.3389/fchem.2020.00042.
40 M. Durai, S. Kumaravel, A. Mukannan, B. Krishnakumar, S. Thiripuranthagan and Y.-H. Ahn, *J. Porous Mater.*, 2021, **28**, 1907–1917.